Insights into the Micro-Structure-Transport Relationships of the Fluoride-Ion Conductor t-$BaSnF_4$ Synthesized by Spark Plasma Sintering

Mercadier, Briséïs; Legein, Christophe; Body, Monique; Famprikis, Theodosios; Morcrette, Mathieu; Suard, Emmanuelle; Masquelier, Christian; Dambournet, Damien

DOI
10.1021/acs.chemmater.4c01644

Publication date
2024

Document Version
Final published version

Published in
Chemistry of Materials

Citation (APA)
Mercadier, B., Legein, C., Body, M., Famprikis, T., Morcrette, M., Suard, E., Masquelier, C., & Dambournet, D. (2024). Insights into the Micro-Structure-Transport Relationships of the Fluoride-Ion Conductor t-$BaSnF_4$ Synthesized by Spark Plasma Sintering. *Chemistry of Materials*, *36*(16), 8076-8087. https://doi.org/10.1021/acs.chemmater.4c01644

CHEMISTRY OF MATERIALS

pubs.acs.org/cm

Article

Insights into the Micro-Structure-Transport Relationships of the Fluoride-Ion Conductor *t*-$BaSnF_4$ Synthesized by Spark Plasma Sintering

Briséïs Mercadier, Christophe Legein, Monique Body, Theodosios Famprikis, Mathieu Morcrette, Emmanuelle Suard, Christian Masquelier, and Damien Dambournet*

Cite This: *Chem. Mater.* 2024, 36, 8076−8087

Read Online

ACCESS | Metrics & More | Article Recommendations | Supporting Information

ABSTRACT: The tetragonal ordered form of $BaSnF_4$ is of particular interest, as its ionic conductivity is high enough to enable its uses as an electrolyte in all-solid-state fluoride-ion batteries. Despite several studies related to its synthesis, structure, and fluoride-ion diffusion mechanism, reported routes often yield impurities as well as unexplained variation in the unit-cell *c*-axis length. Here, we report on the single-phase synthesis of *t*-$BaSnF_4$ via spark plasma sintering, a method that could be used to prepare bulk-type all-solid-state inorganic batteries in one step. By optimizing different parameters (temperature, setup features, etc.), we reached a high ionic conductivity of 5×10^{-3} $S \cdot cm^{-1}$ at 30 °C. In addition, we show that two main factors affect the ionic conductivity. First, on a microstructural scale, the preferential growth of crystallites along the *c*-axis results in a decrease of the ionic conductivity of resulting powders because of the two-dimensional (2D) fluoride-ion diffusion in this material. Second, on the atomic scale, the increase of the unit-cell *c*-axis length is concomitant with a decrease of the ionic conductivity. A combined neutron diffraction and ^{19}F solid-state magic angle spinning (MAS) NMR study reveals that the observed increase of the unit-cell *c*-axis length is due to the partial occupancy of octahedral interstitial sites. NMR allows us to identify these interstitial sites (the F4 site) with distinct isotropic chemical shift values. Furthermore, variable-temperature ^{19}F solid-state MAS NMR reveals that these F4-ions do not exchange with fluoride-ions (F1 and F3) that are responsible for the transport properties. Hence, the occupancy of these interstitial sites tends to lower the 2D fluoride-ion conductivity, and the unit-cell *c*-axis length can be used as a guideline to ensure the preparation of highly conductive samples provided that the microstructure is controlled. Overall, this study provides a novel route to prepare pure *t*-$BaSnF_4$ while establishing a better understanding of the factors affecting its transport properties.

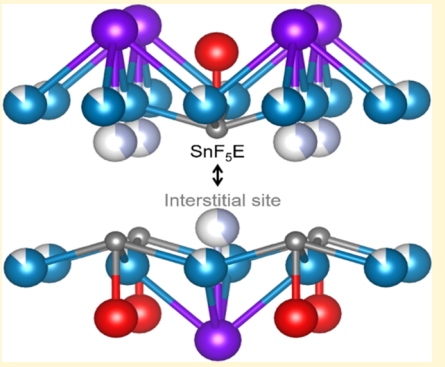

INTRODUCTION

As next-generation solid-state batteries are being developed, anionic fluoride-ion charge carriers present an interesting opportunity that could lead to significant breakthroughs in terms of energy density (capacity and voltage).[1] Fluoride stands at the very end of the standard potential series (+3.05 V vs SHE) and can participate in conversion reactions, giving a theoretical volumetric energy density for fluoride-ion batteries as high as 5000 Wh/L.[1] The high electronegativity of the fluoride-ion means that it is considered a suitable and stable charge-transfer ion. Most remarkably, fluoride-ion batteries are, by nature, dendrite-free systems, providing a compelling option for developing intrinsically safe all-solid-state batteries.

Initial work on the development of fluoride-ion batteries (FIBs) began in the 1970s with the investigation of the electrical properties of fluoride electrolytes (mainly PbF_2) along with unsuccessful attempts to build "fluoride galvanic cells".[2−7] Research into intercalation batteries over the past decades, however, has focused predominantly on lithium-ion and sodium-ion chemistries, and work toward fluoride-ion systems has been limited. It was only in 2011 that Fichtner's group succeeded in operating an all-solid-state FIB, providing the first proof-of-concept.[8] In that work, the FIB was comprised of $La_{0.9}Ba_{0.1}F_{2.9}$ as the solid electrolyte, of conversion-based metal fluorides (CuF_2, BiF_3, SnF_2) as active cathode materials, and of Ce metal as the anode. Following the work of Fichtner et al., other groups worldwide have contributed to the development and optimization of cell designs (bulk,[9] microbatteries[10,11]) and to the screening of conversion-based electrodes[12,13] and redox reaction mechanisms.[10,11,14−17] Several interesting studies report on fluoride intercalation chemistry,[18−22] electrochemical electron−anion

Received: June 12, 2024
Revised: July 23, 2024
Accepted: July 24, 2024
Published: August 7, 2024

exchange in electride materials,[23,24] and electrode/electrolyte interface properties occurring in thin film FIBs.[10,11,25] Finally, a sizable part of the FIB body of work is centered around solid (tysonite,[26−33] fluorite,[34−38] perovskite[39] structural archetypes, and search for generalized material design principles highlighting cation polarizability[40]) and liquid electrolytes.[41,42]

The first solid-state fluoride-ion conductors to be identified and studied were fluorite-derived compounds, such as CaF_2 and PbF_2. The anion transport in these structures requires anionic point defects, either thermally generated anion Frenkel pairs or excess anion interstitials formed in response to supervalent cation doping.[27,29,31,43−45] Activation energies for defect formation and diffusion are typically high, giving these binary fluorite-structured systems relatively low ionic conductivities:[46] CaF_2 has an estimated room-temperature conductivity of $\sigma_{RT} \approx 8 \times 10^{-18}$ S·cm^{-1}, and PbF_2 has $\sigma_{RT} = 2 \times 10^{-8}$ S·cm^{-1}.

The introduction of Sn(II) within the fluorite structure MF_2 yields a significant increase in the ionic conductivity. For example, it is multiplied by a factor of 1000 from BaF_2 to the cubic form of $BaSnF_4$, i.e., Sn and Ba occupy the same crystallographic site through the effect of a combined lone pair and fluoride-ion disorder dynamics.[47] Because there is no continuous percolating diffusion pathway in the cubic phase, the transport properties are still far from those required for a solid electrolyte. The ordered polymorph of $BaSnF_4$, on the other hand, features higher conductivities, ranging from 3.5×10^{-4} to 7.2×10^{-3} S·cm^{-1} at 30 °C,[34,48−50] compatible with their use in an electrochemical cell.[34,51] This compound crystallizes in the tetragonal $P4/nmm$ space group and consists of Ba and Sn layers, in a Sn−Ba−Ba−Sn sequence, connected by fluoride-ions. The Sn−Sn interlayer is void of any F^- ion because the tin's $5s^2$ electrons stereoactive lone pair points toward the c-direction and takes up the space of a fluoride-ion in the tin coordination sphere (Figure 1).[52] According to the findings of an in-depth solid-state NMR study,[53,54] the transport properties of t-$BaSnF_4$ result from both the two-dimensional (2D) motions of fluoride-ions between the Ba and Sn layers, and the few fluoride-ions hypothesized to be located within the Sn−Sn layers.

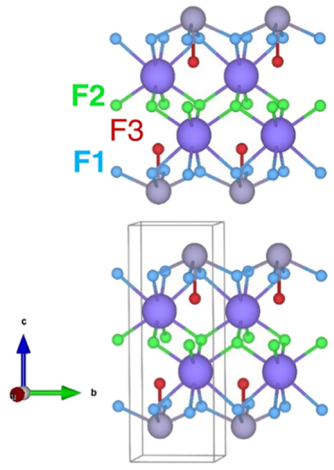

Figure 1. Structural representation of the ordered tetragonal phase $BaSnF_4$. Barium and tin are represented in purple and grey, respectively. The three labeled F sites are represented in blue (F1), green (F2), and red (F3).

t-$BaSnF_4$ was first prepared by solid-state synthesis: stoichiometric amounts of BaF_2 and SnF_2 were ground and heated to 500 °C in a sealed copper tube under N_2.[50] Subsequently, a number of synthesis routes were reported, ranging from coprecipitation[55−57] to high-temperature synthesis,[53,56] and finally a combination of mechanochemical-milling and heat treatments.[39,49,56,58]

Table 1 gathers the reported t-$BaSnF_4$ cell parameters and volume for the aforementioned synthesis routes. Interestingly, the unit-cell c-axis lengths vary drastically, from 11.228(1) to 11.3752(9) Å, from one synthesis route to another. Note that the same phenomenon is observed for the $PbSnF_4$ isomorph, with unit-cell c-axis lengths varying from 11.415 Å to 11.744(32) Å.[59,60] This may affect the overall transport properties but has never been investigated. Moreover, the materials obtained are often not pure, the final product consisting of a mix of a tetragonal phase with a cubic impurity (Table 1). The structure of the cubic impurity is similar to that of BaF_2, but its composition is unknown, as Sn may be introduced in BaF_2 fluorite without causing cell expansion or contraction.[47,58] Therefore, the final product of such syntheses could be more accurately described as a mixture of t-$Ba_{1+x}Sn_{1-x}F_4$ and c-$Ba_{2-x}Sn_xF_4$.

Motivated by the possibility to prepare a bulk-type all-solid-state inorganic batteries in a one step,[61] we used spark plasma sintering (SPS) method to synthesize pure t-$BaSnF_4$. By optimizing the synthesis parameters, we reached a high ionic conductivity of 5×10^{-3} S·cm^{-1} at 30 °C and attempted to correlate particular microstructural properties obtained by SPS to ionic conductivities. In addition, we analyzed in depth the structural features of the synthesized compounds and suggested that the unit-cell c-axis length variation is correlated with the occupancy of interstitial sites by F-ions. Although several parameters can be at stake, the occupancy of this site being associated with a lower conductivity, the unit-cell c-axis length can be used as a guideline to prepare a high fluoride-ion conductor. Lastly, we investigated the electrochemical chemical stability window and showed that $BaSnF_4$ is sufficiently stable for its use in a battery, in good agreement with the work of Chen et al.[62]

MATERIALS AND METHODS

SPS Synthesis. At first, BaF_2 and SnF_2 powders were mixed in stoichiometric proportions through ball milling as detailed in ref 47. Briefly, powder precursors (SnF_2, Sigma-Aldrich, 99%; BaF_2, Sigma-Aldrich, 99.99%) were weighed and sealed in zirconia milling jars in an argon-filled glovebox, with a powder-to-ball ratio of 1:13. The balls were 10 mm in diameter and were made of zirconia. The precursors were then milled at 400 rotations per minute for 12 h, divided in 24 cycles. Each cycle consisted of 15 min of milling and 15 min of pause to prevent overheating. Then, the SPS synthesis was first attempted using the protocol previously developed in-house for other materials.[63,64] SPS dies were lined with carbon paper (Papyex) and dried in an oven at 70 °C for a few hours. Inside the glovebox, around 450 mg of precursor powder was added to the die and pressed into pellets using an uniaxial press. Dried Papyex discs were then added to both sides of the pellet, and a thin layer of carbon powder was added after pressing, before the stack was placed in the SPS apparatus.

After the synthesis, the pellets were removed from the dies and polished until their surface was even with 2000 and 5000 grit polishing papers. The Papyex discs adhered to the materials and were kept as semiblocking electrodes for electrochemical impedance spectroscopy (EIS) measurements, before being polished off for powder X-ray diffraction (XRD) measurements Note that carbon

https://doi.org/10.1021/acs.chemmater.4c01644
Chem. Mater. 2024, 36, 8076−8087

Table 1. Literature Survey of the Reported Cell Parameters and Phase Purity for *t*-$BaSnF_4$. BM = Ball Milling, HT = Heat Treatment, C = Coprecipitation

aynthesis method	*a* (Å)	*c* (Å)	*V* (Å^3)	phase purity	refs
BM&HT	4.345(1)	11.228(1)	211.97	cubic impurity (7.6 wt %)	58
BM& HT	4.3337(4)	11.2273(10)	211.02	pure $Ba_{0.86}Sn_{1.14}F_4$	49
	4.3356(6)	11.2280(16)	211.05	$Ba_{0.94}Sn_{1.06}F_4$ + cubic impurity	
BM& HT	4.35	11.28	213.44	cubic impurity	56
HT	4.3564(6)	11.289(2)	214.2(1)	unreported	50
C	4.348(5)	11.243(3)	212.6	cubic impurity	56
C&HT	4.3538(2)	11.3752(9)	215.62(2)	pure	57

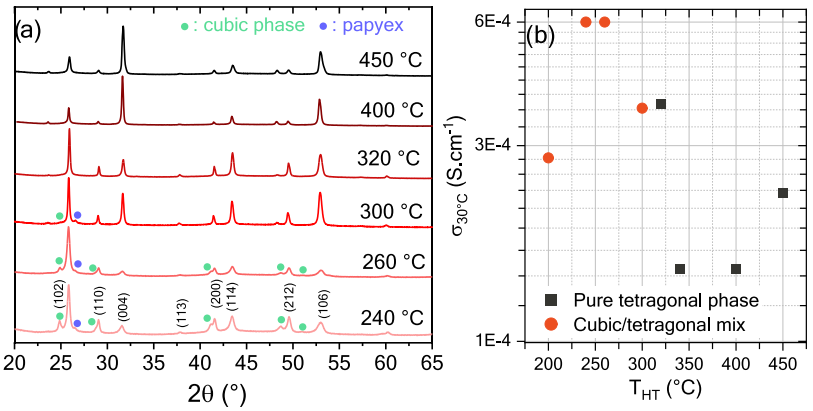

Figure 2. Effect of the SPS synthesis temperature (HT: heat treatment) on (a) the powder XRD patterns of the obtained pellets. The blue stars mark the presence of carbon paper (Papyex) that was not polished off completely because of the high pellet fragility and (b) the ionic conductivity measured at 30 °C.

diffusion inside the material is sometimes an issue when using SPS but was not observed here, as the pellets remained pure white.

For comparison purposes, we synthesized a sample with a specific modified ball-milling method (284 cycles) and two annealing steps performed at 300 °C for 3 h under Ar. This sample features a large unit-cell *c*-axis length. Characterizations can be found in the (Supporting Information) (SI).

Powder X-ray and Neutron Diffraction. Powder X-ray diffraction was performed using a Bruker D8 Advance powder diffractometer with a copper anode (Cu−Kα = 1.5418 Å). Measurements were performed on unground pellets. The powder XRD pattern was fitted using the Rietveld method as implemented in the Fullprof program,[65] with a split pseudo-Voigt function to model the peak shape.[66]

Neutron powder diffraction data were collected on the PEARL neutron powder diffractometer at the research reactor of TU Delft.[67] Approximately 3 g of sample was loaded on a 6 mm diameter cylindrical V−Ni null-scattering alloy can, which was in turn placed in a neutron-transparent vacuum box connected to a primary vacuum (~ 10^{-3} mbar). Measurements of the powder sample were collected at room temperature with a neutron wavelength of 1.667 Å selected using the 533 reflection of a Ge[511] monochromator. To obtain a large content of sample, a pellet of 3.5 g was treated under SPS at 380 °C for 15 min followed by a second treatment at 340 °C for 3 h to ensure the phase purity.

Impedance Spectroscopy. Electrochemical impedance spectroscopy was performed on *t*-$BaSnF_4$ pellets coated with gold. Measurements were performed with a BioLogic MTZ-35 impedance analyzer with data collected in a frequency range of 3.5×10^7 to 1 Hz under an Ar atmosphere.

Electrochemical Stability Window. Measurements were performed using an in-house solid-state battery setup, which consists of a matrix encapsulating two pistons under controlled pressure and atmosphere. First, 120 mg of $BaSnF_4$ was pressed at 1.5 tons in a uniaxial press. For the electrodes, $BaSnF_4$/VGCF composites were prepared by grinding (with a mortar and pestle) 30 mg of $BaSnF_4$ with 10 mg of VGCF. Ten mg of this composite was then added to one side, while 10 mg of the Pb/PbF_2/VGCF composite was added on the other side. The stack was pressed again at 1.5 ton, put under a pressure of 20 kN, and sealed under an argon atmosphere.

^{19}F NMR. ^{19}F magic angle spinning (MAS) NMR experiments were performed on Bruker Avance III spectrometers operating at B_0 = 7.0 T (^{19}F Larmor frequency of 282.4 MHz), using a 1.3 mm CP-MAS probe head. The ^{19}F MAS spectra were recorded in direct polarization (single 90° pulse) and using a rotor-synchronized Hahn echo sequence with an interpulse delay equal, by default, to one rotor period. The 90° pulse length and the recycle delay were set to 1.63 and 60 s, respectively. ^{19}F spectra are referenced to $CFCl_3$, and they were fitted by using the DMFit software.[68]

RESULTS AND DISCUSSION

Synthesis of Single-Phase *t*-$BaSnF_4$. "Spark plasma sintering" (SPS) is a pressure and electric current-assisted sintering/synthesis technique. DC current millisecond pulses are sent through powders, heating it via the Joule effect, while it is kept under uniaxial pressure. It is akin to a hot press, although heat originates from the current, which is thought to provide additional benefits in terms of sintering kinetics. The combination of current and pressure allows for efficient sintering, often at temperatures between 200 and 500 °C, i.e., lower than required by regular high-temperature processing routes. The sintering times are also significantly shorter.[69] One of the attractive features of SPS is its high heating and cooling rates, reaching up to 1000 and 150 K·min^{-1}, respectively.

The first synthesis attempts were made by holding the $BaSnF_4$ sample for 30 min at 300 °C, the temperature previously used for conventional heat treatments. There was a small amount of cubic impurity left, enough for the most intense peak (111) of this phase to be visible but not for it to

https://doi.org/10.1021/acs.chemmater.4c01644
Chem. Mater. 2024, 36, 8076−8087

be accurately quantified by the Rietveld refinement. In order to improve the phase purity, we first tried to change the holding time: increasing it to 45 min or 1 h and decreasing it to 15 and later 5 min did not prevent the appearance of the cubic impurity. Interestingly, the material held for only 5 min at 300 °C had a purity similar to that of the others. Faster and slower ramps were also tested and did not influence the purity. All resulting pellets were characterized using powder XRD and indexed to *t*-$BaSnF_4$. Le Bail refinements of resulting diagrams showed that they all had different cell parameters, with some significant variations of the *c*-parameter, though the variation did not follow any trend concerning holding time.

The greatest effect on the final purity of the sample was obtained by varying the synthesis temperature, as shown in Figure 2a. The weight percent of cubic phase was determined through the Rietveld analysis for each sample, going from 18.4(9) wt % for the sample synthesized at 240 °C down to 5.8(3) wt % for the one at 260 °C, reaching unquantifiable quantities from 300 to 360 °C and completely disappearing from 400 °C on. When investigating the transport properties of these materials, however, it was found that higher purity did not necessarily result in higher conductivity. As seen in Figure 2b, the best conductivity for this series of experiments was obtained for mixed cubic/tetragonal phases, with below 10% cubic impurity in the final materials. We did not expect it to be so, given the higher bulk conductivity of the tetragonal phase compared to any tin-containing $Ba_xSn_{2-x}F_4$ fluorites.[70] Additionally, in most ceramics, higher sintering temperatures generally result in lower porosity and hence better global ion transport. Here, the measured conductivity mostly decreases when the annealing temperature increases, suggesting that other factors such as the microstructure play a significant role, which is detailed in the next part.

Influence of Synthesis Temperature on the Microstructure of $BaSnF_4$. In order to find a possible explanation for the conductivity variation as a function of annealing temperature, we further characterized the microstructure, first through compacity measurements. Compacity is defined as the ratio between the experimental density and the theoretical density. For many ceramics, the sintering temperature has a dramatic effect on pellet compacity and, consequently, on the conductivity. We could, however, not link higher compacity with higher synthesis temperatures. Compacities ranged from 84 to 94%, but higher compacities did not always mean higher conductivities in this case.

Similarly, synthesis temperatures normally impact particle size, which should, in turn, influence conductivity. We therefore evaluated the crystallite domain sizes using Williamson−Hall diagrams[71] based on

$$\beta \cos \Theta = \lambda/L + 4\varepsilon \sin \Theta$$

where β is the integral breadth of the peak (integral intensities), Θ is the diffraction angle (in radian), λ is the wavelength of the diffractometer radiation, L is the crystallite size, and ε is the rate of microstrain ($\varepsilon = \Delta d/d$, with d being the interplanar distance and Δd being the local variations introduced in the material by distortions).

It should be noted that diffractograms measured on either side of the same pellet often displayed slight differences, and therefore, in order to accurately evaluate the impact of various synthesis parameters on the microstructure, we measured both sides, except when the fragility of the pellets prevented us from doing so. Most often, the top side, which was exposed to the current first, had more anisotropic crystallites and stronger preferential orientations.

Generally, the Bragg peaks get progressively wider as 2Θ increases, and the product of the integral breadth and the cosine of the angle, i.e., Williamson−Hall plot, forms a line, from which the crystallite size and the microstrain may be deduced. As shown in Figure 3, this behavior is indeed

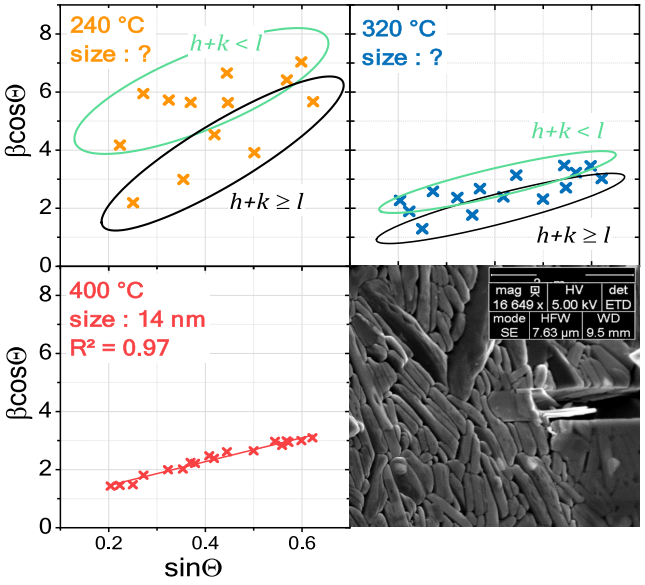

Figure 3. Left and top right: Williamson−Hall diagrams of *t*-$BaSnF_4$ SPS synthesized at different temperatures. The black and green circles encompass planes where $h + k \geq l$ and $h + k < l$, respectively. Bottom right: SEM image of a pellet piece after SPS synthesis at 320 °C shows the platelet shape.

observed for samples synthesized at high temperature (T_{SPS} > 380 °C). However, as the synthesis temperature lowers, the relationship is no longer linear. The distribution of points in the Williamson−Hall diagrams of these materials becomes cloudlike, with $h + k \geq l$ at the bottom and $h + k \geq l$ above. Even with this distinction, it was not possible to estimate strain or crystallite size in either direction because the R^2 value of the linear fits was too small (e.g., for 240 °C, 0.79 for the bottom part and 0.43 for the top part). Overall, the trend seems to point to larger and more strained crystallites in high [hk] directions. This anisotropy was also present at the particle level, as seen on scanning electron microscopy (SEM) images (Figure 3) from a sample synthesized at 320 °C presenting platelet-shaped particles. A higher temperature yielded less anisotropic and somewhat smaller crystallites: 14 nm for 400 °C and 8 nm for 450 °C. This might be explained by a partial decomposition/recrystallization of the compound as suggested by the previous differential scanning calorimetry measurement, showing that *t*-$BaSnF_4$ normally would decompose before 400 °C.[36] We therefore used faster cooling rates, which, in turn, may be responsible for the smaller crystallite sizes.

Another important feature of the XRD diagrams is the evolution of the relative peak intensities as a function of the synthesis temperature. The (102) reflection is the most intense of the calculated diagram[58] of *t*-$BaSnF_4$, and the intensity of the (004) peak is such that $I_{(004)} = 0.13 \times I_{(102)}$. As seen in Figures 2 and4, the relative peak intensities shift dramatically with the synthesis temperature to the point where (004) becomes the most intense reflection of the diagram. Note that

https://doi.org/10.1021/acs.chemmater.4c01644
Chem. Mater. 2024, 36, 8076−8087

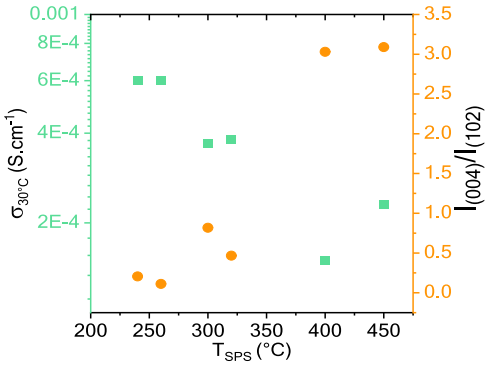

Figure 4. Ionic conductivity (in green) and preferential growth ($I_{(004)}/I_{(102)}$) XRD peak ratio, in orange as a function of the SPS synthesis temperature.

the intensity of its harmonic (002) also grows significantly. In general, all peaks originating from $h + k < l$ planes expand, evidencing an oriented growth of the crystallites. This phenomenon has already been observed for other materials synthesized with SPS, such as Sb_2Te_3,[72] Bi_2Te_3,[73] and Ti_3SiC_2.[74] For the latter, oriented crystallite growth has been related to the applied pressure and high heating rates, but for the former, there may also be an electronic effect induced by the lone pair present on Sb and Bi ions. In our case as well, the tin lone pair may be responsible for the preferential growth since it aligns with the SPS electric field. Indeed, lone pairs are known to rotate to align with electric fields in other materials as well (ferroelectric switching).[75]

It is interesting to note that the degree of crystallographic orientation is here the inverse of the degree of anisotropy of the crystallites. At low synthesis temperature, the crystallographic domains are not oriented (within the pellet) but particles are strongly anisotropic, forming platelets (Figure 5a). As the temperature increases, the domains become smaller and isotropic but the crystallographic planes become more aligned (Figure 5b). This preferential orientation affects the transport properties of the pellet, as the Ba layers hinder F-ion diffusion in the *c*-direction.[54] From these considerations, the optimization of the synthesis to reduce the preferential orientations to a minimum allowed us to obtain a pellet with a high conductivity of 5.10^{-3} S·cm^{-1} at 30 °C.

Attempts to Correlate the Ionic Conductivity to Unit-Cell Parameters. The XRD patterns of the different samples prepared through SPS were analyzed to extract unit-cell parameters, microstructures, and preferential orientations. One noteworthy specificity of these refinements was the use of a Thompson−Cox−Hastings function to model the peak shapes.[66] This function accounts for microstructure, and as such, we were able to more accurately fit the diagrams of heavily oriented samples, which had platelet-shaped crystallites. An example of one such fit is presented in Figure S1.

The crystallographic unit-cell volumes and unit-cell *a*-, *c*-axis lengths were plotted against conductivity measured at 30 °C, seeking potential correlations. Both *a*-parameter, which varies only slightly, and cell volume appear to display a faint correlation with the ionic conductivity (Figure S2). The unit-cell *c*-axis length variation, however, presents a correlation with the ionic conductivity, with lower *c* leading to better transport properties (Figure 6). The origin of such an effect is investigated in the next section.

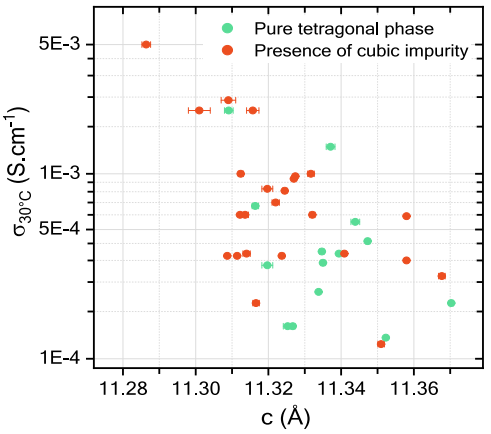

Figure 6. Conductivity of SPS-synthesized *t*-$BaSnF_4$ as a function of the unit-cell *c*-axis length. The data were obtained for all of the samples synthesized in the course of the study including samples prepared with different synthesis temperatures, holding times, cooling rates, or different ball-milling times.

Evidence for the Occupancy of Interstitial Sites. To determine the structural feature affecting the unit-cell *c*-axis length and in turn the ionic conductivity as observed in Figure 6, we conducted a structural analysis on a sample featuring a large unit-cell *c*-axis length using powder neutron diffraction and ^{19}F solid-state MAS NMR. For the sake of context, we recall that the fluoride sublattice of *t*-$BaSnF_4$ was originally described by three anionic sites F1, F2, and F3 occupying 4f, 2b, and 2c Wyckoff positions, respectively. As mentioned above, typical unit-cell *c*-axis lengths are in the range of 11.228(1)−11.3752(9) Å. Considering these three fluoride sites without the presence of interstitial fluoride, a unit-cell *c*-axis length of 11.23 Å was obtained by density functional theory calculations.[76] This suggests that the increase of the unit-cell *c*-axis length can be due to a modification of the fluoride sublattice such as the occupancy of interstitial sites.

The Rietveld refinement of the neutron diffraction pattern was performed using the three anionic sites as the starting

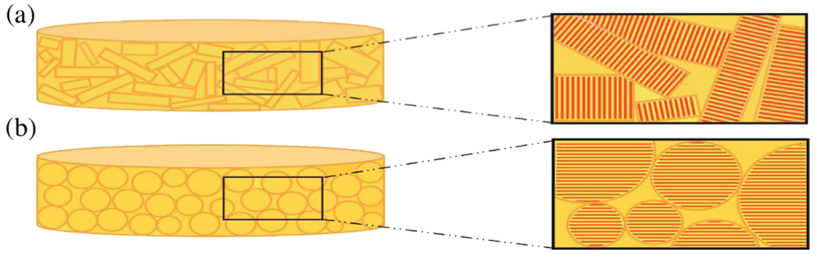

Figure 5. Particle morphology and plane orientation in a pellet sintered in SPS at (a) low and (b) high temperatures.

https://doi.org/10.1021/acs.chemmater.4c01644
Chem. Mater. 2024, 36, 8076−8087

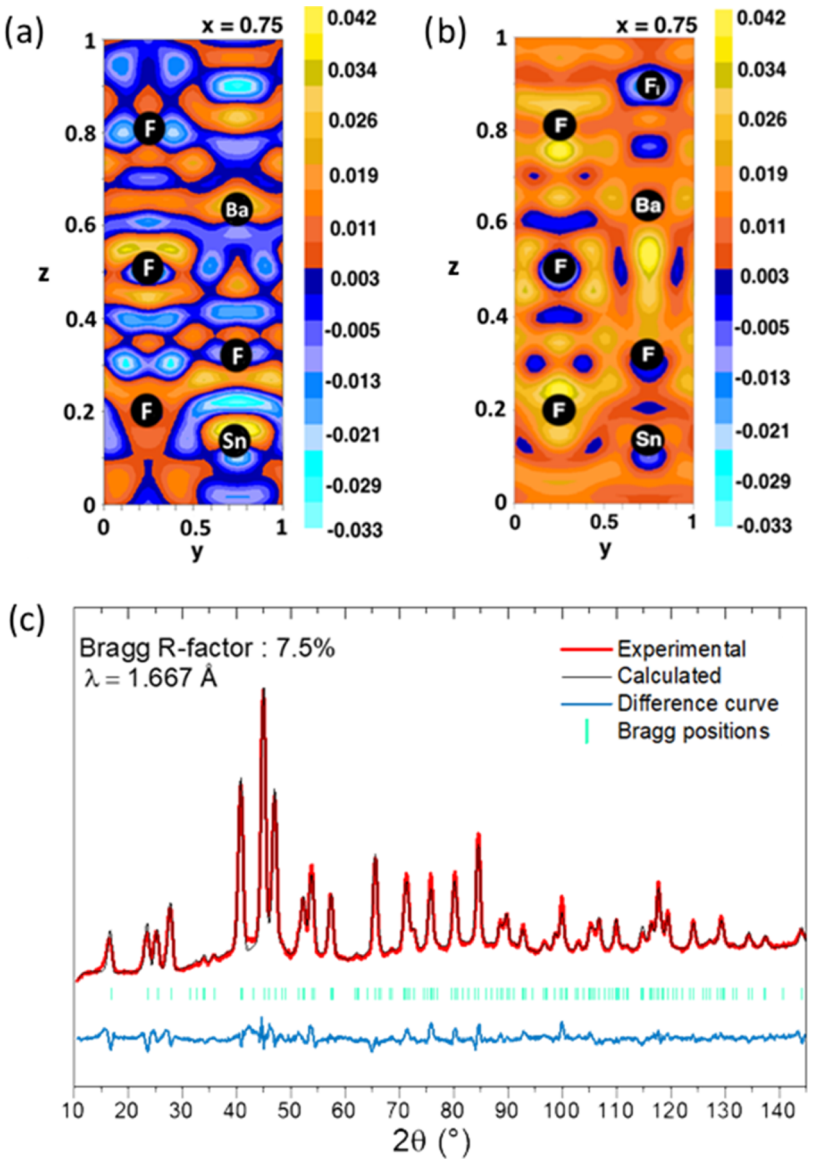

Figure 7. Slices at $x = 0.75$ of the Fourier difference maps (a) without and (b) with the addition of the F4 site. Cold and warm colors show missing and excess nuclear densities, respectively. (c) Rietveld refinement with the additional interstitial F site.

Table 2. Wyckoff Site, Atomic Coordinates, *x*, *y*, and *z*, Atomic Displacement Parameters (U^{ii}, Å^2), and Occupancies Obtained by the Rietveld Refinement of the Neutron Diffraction Data. Space group: *P4/nmm*, *a* = 4.3533(3) Å, *c* = 11.319(2) Å, V = 214.51(6) Å^3

atom	site	*x*	*y*	*z*	U^{11}	U^{22}	U^{33}	Occ.
Ba	2c	1/4	1/4	0.3667(1)	0.010(1)	0.010(1)	0.039(4)	1
Sn	2c	1/4	1/4	0.869(1)	0.031(3)	0.031(3)	0.026(4)	1
F1	4f	3/4	1/4	0.191(1)	0.064(4)	0.064(4)	0.054(6)	0.78(6)
F2	2b	3/4	1/4	1/2	0.013(2)	0.013(2)	0.053(5)	1
F3	2c	1/4	1/4	0.691(1)	0.136(2)	0.136(2)	0.026(4)	1
F4	2c	1/4	1/4	0.109(6)	0.63(6)	0.63(6)	0.20(4)	0.44(9)

model as proposed by Ahmad et al.[58] Fourier maps were then calculated to capture the goodness of the model, and we found that nuclear density was missing on the $x = 0.75$ slice (which mirrors the $x = 0.25$ slice) at $y = 0.75$, $z = 0.25$ (Sn site: lone pair related) and at $y = 0.75$, $z = 0.9$ (empty site) (Figure 7a).

To account for the missing nuclear density, we added an interstitial F site, named F4 thereafter, located within the 2c Wyckoff position. In addition to its z coordinate, the occupancies of this interstitial F4 site, as well as those of the two neighboring F1 and F3 sites, were refined. To compare the goodness of the fit, we calculated Fourier maps showing that the missing nuclear density is now well-captured (Figure 7b). The resulting fit is displayed in Figure 7c. The interstitial F4 site is partially occupied (44(9)%) by a part of the F-ion from the F1 site, which is therefore no longer fully occupied (78(6)%).

https://doi.org/10.1021/acs.chemmater.4c01644
Chem. Mater. 2024, 36, 8076−8087

Several noteworthy information can be extracted from the refinement, including structural parameters (Table 2) as well as selected interatomic distances (Table 3). The fluoride

Table 3. Selected Interatomic Distances (Å) Obtained by the Rietveld Refinement of the Neutron Diffraction Data

Ba	F2 (×4)	2.648	F1 (×4)	2.949	F4 (×1)	2.917
F1	Sn (×2)	2.280	Ba (×2)	2.949		
F2	Ba (×4)	2.648				
F3	Sn (×1)	2.015	Ba (×4)	3.147		
F4	Sn (×1)	2.717	Ba (×1)	2.917	Sn (×4)	3.088

sublattice F1, F2, and F3 bond lengths compare well with literature data,[58] with typical Sn−F bond lengths ranging from 2.03 to 2.28 Å (vs 2.10−2.28 Å[58]). The interstitial F4 (Figure 8) site is located in a large octahedron with equatorial Sn

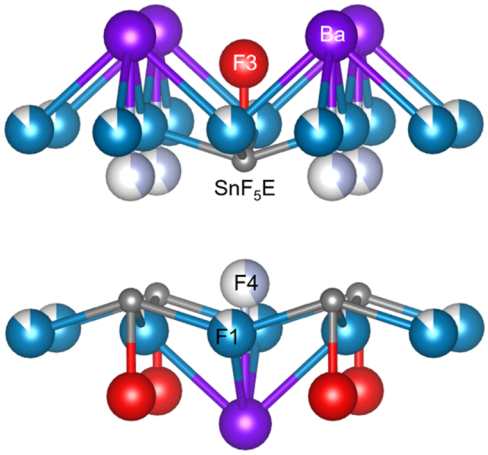

Figure 8. Structural representation showing the local environment of the F4 interstitial.

interatomic distances of 3.08 Å and axial Ba and Sn interatomic distances, along the *c*-axis, of 2.86 and 2.77 Å, respectively. The values of the anisotropic atomic displacement parameters β^{ii} of the F4 site show that the corresponding F-ions are highly delocalized within the equatorial (110) plane, suggesting a static or dynamic disorder. The disorder of this position is inherent since not only is the coordination octahedron (too) large but each F4 site has 4F1 sites as first neighbors at 2.34 Å. It therefore seems likely that when an F4 site is occupied, one of these 4F1 sites is not. So, F-ions occupying an F4 site certainly move away from the occupied F1 sites and toward a Sn−Sn edge in the equatorial plane. The NMR study presented below will allow us to show the dynamic nature of this disorder.

Along the *c*-axis, the F4−Ba bond length suggests an ionic character. However, the distance to Sn is longer than typical Sn−F bonds due to a tin electron lone pair (E) pointing in that direction. Matar et al.[76] estimated the Sn−E distance to be in the range of 0.73−0.77 Å. It can be concluded that the observed increase in the unit-cell *c*-axis length (and the spread value observed in the literature) is caused by the occupancy of the interstitial site that leads to a repulsion effect between these interstitial F-ions and the electron lone pairs. Finally, the broadness of the (00l) Bragg reflection reflects the local structural variations within the *c*-axis induced by the partial occupancy of the interstitial F4 site.

Further confirmation of the partial occupancies of the F1 and interstitial F4 sites and of the resulting disorder, as well as information on F-ion mobilities, was obtained from ^{19}F solid-state NMR spectroscopy. The MAS NMR spectra of the sample synthesized by SPS recorded at different MAS frequencies (from 34 to 60 kHz) and the fit of the latter are presented in Figures 9 and10 and Table 4, respectively. The fits

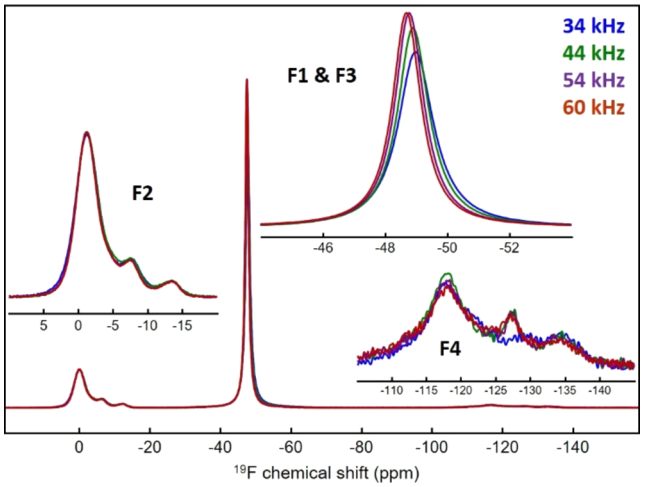

Figure 9. ^{19}F MAS NMR spectra of *t*-$BaSnF_4$ recorded at 34 (blue), 44 (green), 54 (mauve), and 60 kHz (red). The three main contributions are assigned and enlarged.

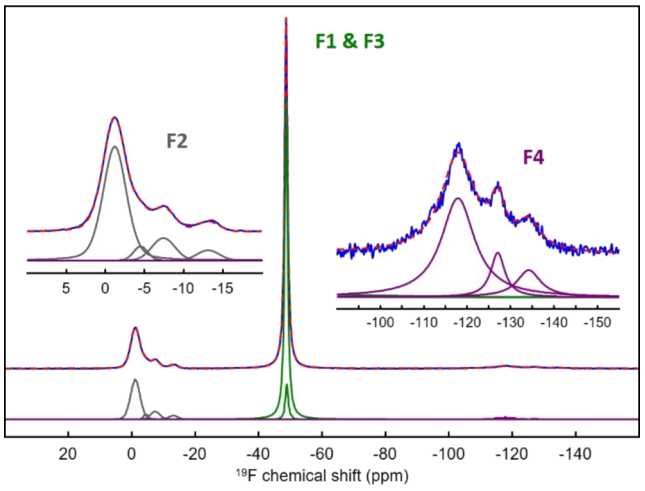

Figure 10. ^{19}F MAS (60 kHz) NMR spectrum of *t*-$BaSnF_4$ (in blue), its fit (in dash red), and below the individual resonances used for the fit (Table 4). The three main contributions are assigned, and those assigned to F2 and F4 are enlarged.

of the other spectra are given in the SI (Figures S3, S5 and Tables S1−S3). These spectra have similarities but also some differences from those reported by Chaudhuri et al.[54] for a sample prepared by solid-state reaction. The spectra of both the compounds show two main contributions, at δ_{iso} = −3 and −49 ppm, convincingly assigned,[54] based on their relative intensities and on the δ_{iso} values of ^{19}F in BaF_2 (−14 ppm) and SnF_2 (−44 and −51 ppm[47]), to F-ions in the Ba^{2+} double layers (referred to as F2) and between the Ba^{2+} and Sn^{2+} layers (referred to as F1 and F3), respectively.

The resonance at δ_{iso} = −49 ppm accounts for F1 and F3 sites with different environments, themselves distributed, given

https://doi.org/10.1021/acs.chemmater.4c01644
Chem. Mater. 2024, 36, 8076−8087

Table 4. Isotropic Chemical Shifts (δ_{iso}, ppm), Line Widths (LW, ppm), and Relative Intensities (I,%) of the ^{19}F NMR Lines Used for the Fit of the ^{19}F MAS NMR Spectrum of t-$BaSnF_4$, and Assignment of These Lines to the Three Types of Fluorine Atoms and the Corresponding Relative Intensities (ΣI,%) and Weighted Average δ_{iso} Values ($\langle\delta_{iso}\rangle$, ppm)

δ_{iso}	LW	I	assignment	ΣI	$\langle\delta_{iso}\rangle$
−134.2	6.6	0.79		5.6	
−127.0	3.9	0.76			
−117.9	9.3	4.04	F4		−121.4
−49.0	1.1	6.7		68.4	
−48.7	1.1	61.7	F1&F3		−48.7
−13.1	3.4	1.4		26.0	
−7.4	3.5	3.4			
−4.5	2.1	1.3			
−1.2	3.5	20.0	F2		−2.8

the disorder resulting from the partial occupancies of the F4 and F1 sites. The observation of a single, motionally averaged resonance (almost perfectly symmetrical, narrow, with a Lorentzian line shape and weak spinning sidebands) indicates that the F-ions between the Ba^{2+} and Sn^{2+} layers must be undergoing very rapid jumps between the different sites, with a rate $k = 1/\tau_c$, where τ_c is the correlation time associated with the motion, which Chaudhuri et al.[54] estimated to be close to 10^{-8} s at RT.

The resonance at −3 ppm was assigned by Chaudhuri et al.[54] to the F-ions located in the Ba^{2+} double layers, forming a rigid sublattice on the MAS NMR time scale at RT. While this resonance appears symmetrical for their sample, the contribution from our sample is not, spreading over more than 10 ppm and requiring four Gaussian lines to be perfectly reproduced (Figures 10, S3−S5 and Tables 4, S1−S3). The sum of the relative intensities of the four lines assigned to F2-ions, close to 25%, supports this assignment. This distribution of ^{19}F δ_{iso} values for F2-ions is related to the various environments experienced by Ba^{2+} ions as further discussed below.

Remarkably, our spectrum features as additional contribution, which is absent in the study of Chaudhuri et al.[54] Such additional contribution is of low intensity spreading over about 20 ppm and whose average chemical shift is significantly lower than that of the F1- and F3-ions, indicating overcoordinated F-ions[77] (Table 4), i.e., coordination number greater than 4. Taken together, these elements allow us to assign it to the interstitial F4-ions detected by neutron diffraction. In addition, this site experiences three distinct environments (Table 4), which can be related to the statistical distribution of vacancies in the 4F1-ions surrounding the F4 site. It is likely that the short F1−F4 distance (2.4 Å) induces an off-center displacement of the F4-ion toward an F1-vacancy, in good agreement with the high anisotropic atomic displacement within the equatorial (110) plane obtained by neutron diffraction.

Interestingly, these different fluorine environments originating from the occupancy of the F4 site and F1-vacancy affect the F2 environments as shown by the detection of three types of resonances (Table 4).

The relative intensity of the F4-ion (∼6%; Tables 4 and S1−S3) does not evolve significantly from ∼30 to ∼55 °C, with the temperatures of the sample in the rotor spinning at 34 and 60 kHz, respectively. We can therefore conclude that the F4-ions do not exchange with the F1 and F3 ones. Comparing the rate occupancy of the F4 site by neutron (11%) and NMR (6%), a slight difference is observed and NMR is assumed to be more sensitive than neutron diffraction, especially for such a low content.

Variable-temperature spectra (34−60 kHz, i.e., from ∼30 to ∼55 °C) further confirm the observation by Chaudhuri et al.[54] on F1 and F3 sites. It shows that when increasing the temperature, the width of the resonance assigned to F1 and F3 decreases, suggesting that the fast exchange regime is about to be reached and its average δ_{iso} value increases, indicating that the average fluorine environment changes with temperature. Since an increase in temperature generally leads to an increase in interatomic distances and thus to a decrease in the chemical shift of ^{19}F, this implies that the time spent by the mobile F-ions in the different F sites changes as a function of temperature since new sites do not become occupied as the temperature increases.[54]

Finally, spectra (Figure S6) were recorded using the Hahn echo sequence rotor-synchronized to a variable number of rotor rotation periods (from 1 to 8), i.e., acquired after a variable dead time. The intensity of the F1, F3, and F4 lines decreases, while that of the F2 line remains unchanged. Spin−spin relaxation (transverse relaxation) and loss of spin coherence are therefore faster for F-ions occupying the F1, F3, and F4 sites. This was expected for the most mobile F1,F3-ions, and this shows the dynamic nature of the disorder of the interstitial F4 site within the equatorial plane of its large coordination octahedra, certainly enhanced by its changing environment related to the exchange of F1- and F3-ions.

In conclusion, the ^{19}F MAS NMR spectra of our t-$BaSnF_4$ sample show an additional contribution assigned to the fluoride-ions occupying the F4 interstitial site. The ions occupying this site no longer exchange with the highly mobile F1- and F3-ions and, therefore, perturb the 2D diffusion pathway. The contributions from the F4 and F2 sites show that their environments are distributed due to the disorder generated by the partial occupation of the F1 and F4 sites.

Discussing Factors Affecting the Ionic Conductivity. Within the same class of materials, ionic conductivity values can vary from several orders of magnitude, mostly depending on the preparation methods, which can affect the microstructure and structure. The former includes the degree of densification, particle morphology/orientation/grain size, and the presence of amorphous content, while the latter includes changes of local structure and occurrence of structural disorder.[78] Herein, we have demonstrated that the microstructure can affect the transport properties due to the 2D nature of fluoride-ion diffusion. To further advance on the understanding of the various factors that can affect t-$BaSnF_4$ transport properties, we considered another sample prepared with a modified mechano-milling synthesis (see the Materials and Methods Section) that yield a tetragonal phase with a particularly large c-axis length, aiming to understand the link between the ionic conductivity value and the unit-cell c-axis length/F4 occupation. The Le bail profile refinement (Figure S7) yielded the corresponding unit-cell parameters a= 4.3630(5) and c = 11.410(4) Å. The ionic conductivity at 30 °C was 7.17×10^{-5} S·cm^{-1} (Figure S8). This value is among the lowest value reported for t-$BaSnF_4$, which is typically spread from 3 to 7×10^{-4} S·cm^{-1} for stoichiometric $BaSnF_4$ prepared by a combined ball milling/heat treatment.[36,56,58] When plotting this value with the data gathered in Figure 6

https://doi.org/10.1021/acs.chemmater.4c01644
Chem. Mater. 2024, 36, 8076−8087

(see Figure S9), it further supported the link between the *c*-axis length and the ionic conductivity, i.e., a large *c*-axis length correlates with a low ionic conductivity. In addition, this sample features a higher proportion of the F4 site as revealed by a larger relative intensity of the resonance assigned to F4- ion (~10%; Figure S10 and Table S4), showing that the presence of interstitial sites increases the repulsive strength with the tin lone pair within the *c*-direction, yielding to an increase of the *c*-axis length.

Another factor affecting the ionic conductivity is the deviation of the nominal phase composition of $BaSnF_4$. In the work of Mori et al.,[49] Sn-rich compositions were prepared and analyzed by neutron diffraction. A pure phase could be synthesized, suggesting that some Ba^{2+} were substituted by Sn^{2+}. The synthesized compounds featured a reduced *c*-axis length, suggesting that cationic intermixing can cause a contraction along the *c*-axis. It is, however, unclear how Sn atoms, particularly the lone pair, locally arrange in the Ba layer.

Finally, we noted that the highest value,[50] i.e., 7.2×10^{-3} S·cm^{-1} at 30 °C, reported for *t*-$BaSnF_4$ was obtained by solid-state synthesis that included a two-step treatment at 200 and 500 °C in a sealed copper tube. Owing to its oxophilic nature, the use of copper can reduce traces of oxygen, which can eventually yield high-purity materials. This suggested that working in a strictly dried atmosphere is critical to obtain a highly conductive phase.

Overall, yet many parameters can affect ionic conductivity, we have demonstrated that the *c*-axis length can be used as a guide to prepare highly conductive phase.

Electrochemical Stability. As the main potentially interesting application of *t*-$BaSnF_4$ is as a solid electrolyte, it is important that in addition to its high ionic conductivity, the material also possesses an appropriate electrochemical stability window (ESW), which can be estimated by building a solid-state battery.[79] One of the electrodes of said battery should be a reference with a stable potential, while the other would be a mixture of the tested electrolyte and conductive carbon. A constant current may then be applied to the cell, while the potential evolution is recorded. This method is useful when examining electrolyte degradation, as if the current applied is small enough (only 10 μA·cm^{-2} here); even processes with slow kinetics may be observed.[80]

Here, the reference used is the one previously established by Wang et al.,[39] which is a mixed Pb/PbF_2 electrode, as its voltage-capacity profile has a plateau. Two separate cells were built: one to study electrolyte reduction and one to study oxidation. For a more direct view of the electrochemical stability window, the results of the constant current polarization experiments are plotted as the derivative curves dQ/dV vs V. Each peak then represents a reaction taking place in the electrolyte. As seen in Figure 11, the dQ/dV vs V curves are seemingly flat between −2 and 2.8 V, which represents a fairly large ESW of 4.8 V, much larger than previously reported.[39] Zooming (Figure S11) on the plateau reveals some smaller peaks at −1.1 and 2.2 V, but they represent a capacity minute enough that the electrolyte could be considered stable throughout this 4.8 V window. Future work should be devoted to identifying the exact mechanism through which *t*-$BaSnF_4$ is oxidized and reduced.

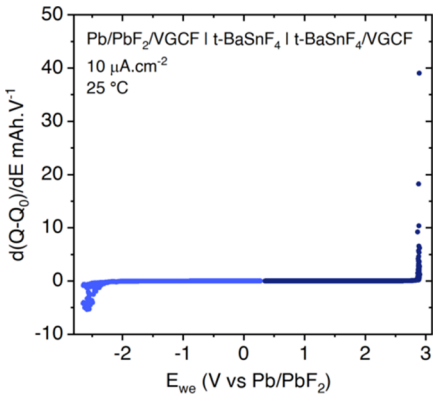

Figure 11. Electrochemical stability window of *t*-$BaSnF_4$, as tested through a solid-state cell Pb/PbF_2/VGCF | *t*-$BaSnF_4$ | *t*-$BaSnF_4$/VGCF. The two colors represent two different cells, one that was exposed to the reductive current and one to the oxidative current (either + or −10 μAh·cm^{-2}). Experiments were conducted at 25 °C.

CONCLUSIONS

In this article, we attempted to prepare pure *t*-$BaSnF_4$ and identify the causes of variations in the cell parameters from one synthesis to another.

We first turned to an original synthesis method, spark plasma sintering, and studied the impact of some of its parameters on the microstructure and conductivity, thereby highlighting two main microstructural effects: crystallite anisotropy for the lower synthesis temperatures and preferential orientation of the crystallites along the high-*l* lattice planes at high temperature. This last effect appears to be the main driving force behind most of the conductivity variations we observed. Highly conductive *t*-$BaSnF_4$ samples, with the value reaching up to 5.10^{-3} S·cm^{-1} at 30 °C, have been prepared by applying optimal synthesis parameters, opening perspectives in the preparation of all-solid-state F-ion batteries assembled by the SPS technique, as for instance previously reported Na-ion batteries.[64]

After characterizing the microstructure and optimizing the synthesis method, we focused on the lattice itself, pointing out the large variations in the unit-cell *c*-axis lengths of the products obtained throughout different synthesis routes. Through refinements of neutron diffraction data, we were able to explain the unit-cell *c*-axis length variations by the occupation, further confirmed by ^{19}F solid-state NMR experiments, of interstitial octahedral sites by part of the F-ions located in the F1 site. The tetragonal phase of $BaSnF_4$ certainly requires further studies in the future, in particular, its anionic sublattice, which contains highly mobile fluoride-ions and may display a degree of disorder.

ASSOCIATED CONTENT

Supporting Information

The Supporting Information is available free of charge at https://pubs.acs.org/doi/10.1021/acs.chemmater.4c01644.

Example of the Le Bail refinement; conductivities vs unit-cell parameters; additional ^{19}F NMR data and spectral reconstruction; detailed characterizations of the sample featuring large unit-cell *c*-axis with the Le Bail profile refinement; Arrhenius plot obtained from electrochemical impedance spectroscopy; conductivity vs unit-cell *c*-axis length of SPS-synthesized *t*-$BaSnF_4$

https://doi.org/10.1021/acs.chemmater.4c01644
Chem. Mater. 2024, 36, 8076−8087

(Figure 6) and the additional sample featuring a large unit-cell *c*-axis length and low conductivity; and ^{19}F NMR spectrum and electrochemical stability window investigation (PDF)

Crystallographic CIF file from neutron diffraction refinement (CIF)

AUTHOR INFORMATION

Corresponding Author

Damien Dambournet − *Réseau Sur le Stockage Electrochimique de l'Energie, RS2E, FR CNRS 3459, 80039 Amiens, France; Sorbonne Université, CNRS, Physicochimie des Electrolytes et Nanosystèmes Interfaciaux, UMR CNRS 8234, 75005 Paris, France;* orcid.org/0000-0003-3831-2643; Email: damien.dambournet@sorbonne-universite.fr

Authors

Briséïs Mercadier − *Réseau Sur le Stockage Electrochimique de l'Energie, RS2E, FR CNRS 3459, 80039 Amiens, France; Sorbonne Université, CNRS, Physicochimie des Electrolytes et Nanosystèmes Interfaciaux, UMR CNRS 8234, 75005 Paris, France; Laboratoire de Réactivité et de Chimie du Solides, UMR CNRS 7314, 80039 Amiens, France*

Christophe Legein − *Institut des Molécules et Matériaux du Mans, UMR 6283 CNRS, Le Mans Université, 72085 Le Mans, France;* orcid.org/0000-0001-7426-8817

Monique Body − *Institut des Molécules et Matériaux du Mans, UMR 6283 CNRS, Le Mans Université, 72085 Le Mans, France;* orcid.org/0000-0002-5895-3731

Theodosios Famprikis − *Department of Radiation Science and Technology, Delft University of Technology, 2629JB Delft, The Netherlands;* orcid.org/0000-0002-7946-1445

Mathieu Morcrette − *Réseau Sur le Stockage Electrochimique de l'Energie, RS2E, FR CNRS 3459, 80039 Amiens, France; Laboratoire de Réactivité et de Chimie du Solides, UMR CNRS 7314, 80039 Amiens, France*

Emmanuelle Suard − *Institut Laue-Langevin (ILL), BP 156, 38042 Grenoble, France;* orcid.org/0000-0001-5966-5929

Christian Masquelier − *Réseau Sur le Stockage Electrochimique de l'Energie, RS2E, FR CNRS 3459, 80039 Amiens, France; Laboratoire de Réactivité et de Chimie du Solides, UMR CNRS 7314, 80039 Amiens, France; Institut Universitaire de France (IUF), 103 boulevard Saint-Michel, 75005 Paris, France;* orcid.org/0000-0001-7289-1015

Complete contact information is available at: https://pubs.acs.org/10.1021/acs.chemmater.4c01644

Funding

B.M., C.M., and D.D. thank the French National Research Agency (STORE-EX Labex Project ANR-10-LABX-76−01) for financial support. Part of this work was supported by a French government grant managed by the Agence Nationale de la Recherche under the France 2030 program, reference 23-PEBA-0002.

Notes

The authors declare no competing financial interest.

ACKNOWLEDGMENTS

T.F. acknowledges the funding provided by the European Union's HORIZON EUROPE programme in the form of a Marie Skłodowska-Curie individual postdoctoral fellowship (project no. 101066486).

REFERENCES

(1) Gschwind, F.; Rodriguez-Garcia, G.; Sandbeck, D. J. S.; Gross, A.; Weil, M.; Fichtner, M.; Hörmann, N. Fluoride Ion Batteries: Theoretical Performance, Safety, Toxicity, and a Combinatorial Screening of New Electrodes. *J. Fluorine Chem.* **2016**, *182*, 76−90.

(2) Kennedy, J. H.; Hunter, J. C. Thin-Film Galvanic Cell Pb/PbF2/PbF2, CuF2/Cu. *J. Electrochem. Soc.* **1976**, *123* (1), No. 10.

(3) Kennedy, J. H.; Miles, R. C. Ionic Conductivity of Doped Beta-Lead Fluoride. *J. Electrochem. Soc.* **1976**, *123* (1), 47−51.

(4) Kennedy, J. H.; Miles, R.; Hunter, J. Solid Electrolyte Properties and Crystal Forms of Lead Fluoride. *J. Electrochem. Soc.* **1973**, *120* (11), No. 1441.

(5) Schoonman, J. A Solid-State Galvanic Cell with Fluoride-Conducting Electrolytes. *J. Electrochem. Soc.* **1976**, *123* (12), 1772−1775.

(6) Schoonman, J.; Wolfert, A. Alloy-Anodes in Fluoride Solid-State Batteries. *J. Electrochem. Soc.* **1981**, *128* (7), 1522−1523.

(7) Danto, Y.; Poujade, G.; Pistré, J. D.; Lucat, C.; Salardenne, J. A Pb|PbF2|BiF3|Bi Thin Solid Film Reversible Galvanic Cell. *Thin Solid Films* **1978**, *55* (3), 347−354.

(8) Reddy, M. A.; Fichtner, M. Batteries Based on Fluoride Shuttle. *J. Mater. Chem.* **2011**, *21* (43), 17059−17062.

(9) Grenier, A.; Gutierrez, A. G. P.; Groult, H.; Dambournet, D. Modified Coin Cells to Evaluate the Electrochemical Properties of Solid-State Fluoride-Ion Batteries at 150 °C. *J. Fluorine Chem.* **2016**, *191*, 23−28.

(10) Nakano, H.; Matsunaga, T.; Mori, T.; Nakanishi, K.; Morita, Y.; Ide, K.; Okazaki, K.; Orikasa, Y.; Minato, T.; Yamamoto, K.; Ogumi, Z.; Uchimoto, Y. Fluoride-Ion Shuttle Battery with High Volumetric Energy Density. *Chem. Mater.* **2021**, *33* (1), 459−466.

(11) Zhang, D.; Yamamoto, K.; Ochi, A.; Wang, Y.; Yoshinari, T.; Nakanishi, K.; Nakano, H.; Miki, H.; Nakanishi, S.; Iba, H.; Uchiyama, T.; Watanabe, T.; Amezawa, K.; Uchimoto, Y. Understanding the Reaction Mechanism and Performances of 3d Transition Metal Cathodes for All-Solid-State Fluoride Ion Batteries. *J. Mater. Chem. A* **2021**, *9* (1), 406−412.

(12) Rongeat, C.; Reddy, M. A.; Diemant, T.; Behm, R. J.; Fichtner, M. Development of New Anode Composite Materials for Fluoride Ion Batteries. *J. Mater. Chem. A* **2014**, *2* (48), 20861−20872.

(13) Thieu, D. T.; Fawey, M. H.; Bhatia, H.; Diemant, T.; Chakravadhanula, V. S. K.; Behm, R. J.; Kübel, C.; Fichtner, M. CuF2 as Reversible Cathode for Fluoride Ion Batteries. *Adv. Funct. Mater.* **2017**, *27* (31), No. 1701051.

(14) Grenier, A.; Porras-Gutierrez, A.-G.; Groult, H.; Beyer, K. A.; Borkiewicz, O. J.; Chapman, K. W.; Dambournet, D. Electrochemical Reactions in Fluoride-Ion Batteries: Mechanistic Insights from Pair Distribution Function Analysis. *J. Mater. Chem. A* **2017**, *5* (30), 15700−15705.

(15) Nowroozi, M. A.; Clemens, O. Insights on the Behavior of Conversion-Based Anode Materials for Fluoride Ion Batteries by Testing against an Intercalation-Based Reference Cathode. *ACS Appl. Energy Mater.* **2018**, *1* (11), 6626−6637.

(16) Haruyama, J.; Okazaki, K.; Morita, Y.; Nakamoto, H.; Matsubara, E.; Ikeshoji, T.; Otani, M. Two-Phase Reaction Mechanism for Fluorination and Defluorination in Fluoride-Shuttle Batteries: A First-Principles Study. *ACS Appl. Mater. Interfaces* **2020**, *12* (1), 428−435.

(17) Zaheer, W.; Andrews, J. L.; Parija, A.; Hyler, F. P.; Jaye, C.; Weiland, C.; Yu, Y.-S.; Shapiro, D. A.; Fischer, D. A.; Guo, J.; Velázquez, J. M.; Banerjee, S. Reversible Room-Temperature Fluoride-Ion Insertion in a Tunnel-Structured Transition Metal Oxide Host. *ACS Energy Lett.* **2020**, *5* (8), 2520−2526.

(18) Nowroozi, M. A.; Wissel, K.; Rohrer, J.; Munnangi, A. R.; Clemens, O. $LaSrMnO_4$: Reversible Electrochemical Intercalation of Fluoride Ions in the Context of Fluoride Ion Batteries. *Chem. Mater.* **2017**, *29* (8), 3441−3453.

(19) Nowroozi, M. A.; Ivlev, S.; Rohrer, J.; Clemens, O. La2CoO4: A New Intercalation Based Cathode Material for Fluoride Ion Batteries with Improved Cycling Stability. *J. Mater. Chem. A* **2018**, *6* (11), 4658−4669.
(20) Nowroozi, M. A.; Wissel, K.; Donzelli, M.; Hosseinpourkahvaz, N.; Plana-Ruiz, S.; Kolb, U.; Schoch, R.; Bauer, M.; Malik, A. M.; Rohrer, J.; Ivlev, S.; Kraus, F.; Clemens, O. High Cycle Life All-Solid-State Fluoride Ion Battery with La 2 NiO 4+d High Voltage Cathode. *Commun. Mater.* **2020**, *1* (1), No. 27.
(21) Wissel, K.; Schoch, R.; Vogel, T.; Donzelli, M.; Matveeva, G.; Kolb, U.; Bauer, M.; Slater, P. R.; Clemens, O. Electrochemical Reduction and Oxidation of Ruddlesden−Popper-Type La $_2$ NiO $_3$ F $_2$ within Fluoride-Ion Batteries. *Chem. Mater.* **2021**, *33* (2), 499−512.
(22) Bashian, N. H.; Zuba, M.; Irshad, A.; Becwar, S. M.; Vinckeviciute, J.; Rahim, W.; Griffith, K. J.; McClure, E. T.; Papp, J. K.; McCloskey, B. D.; Scanlon, D. O.; Chmelka, B. F.; Van der Ven, A.; Narayan, S. R.; Piper, L. F. J.; Melot, B. C. Electrochemical Oxidative Fluorination of an Oxide Perovskite. *Chem. Mater.* **2021**, *33* (14), 5757−5768.
(23) Druffel, D. L.; Pawlik, J. T.; Sundberg, J. D.; McRae, L. M.; Lanetti, M. G.; Warren, S. C. First-Principles Prediction of Electrochemical Electron−Anion Exchange: Ion Insertion without Redox. *J. Phys. Chem. Lett.* **2020**, *11* (21), 9210−9214.
(24) Tojigamori, T.; Matsui, N.; Suzuki, K.; Hirayama, M.; Abe, T.; Kanno, R. Fluorination/Defluorination Behavior of Y2C in Fluoride-Ion Battery Anodes. *ACS Appl. Energy Mater.* **2024**, *7* (3), 1100−1108.
(25) Zhang, D.; Nakano, H.; Yamamoto, K.; Tanaka, K.; Yahara, T.; Imai, K.; Mori, T.; Miki, H.; Nakanishi, S.; Iba, H.; Watanabe, T.; Uchiyama, T.; Amezawa, K.; Uchimoto, Y. Rate-Determining Process at Electrode/Electrolyte Interfaces for All-Solid-State Fluoride-Ion Batteries. *ACS Appl. Mater. Interfaces* **2021**, *13* (25), 30198−30204.
(26) Rongeat, C.; Reddy, M. A.; Witter, R.; Fichtner, M. Nanostructured Fluorite-Type Fluorides As Electrolytes for Fluoride Ion Batteries. *J. Phys. Chem. C* **2013**, *117* (10), 4943−4950.
(27) Chable, J.; Dieudonné, B.; Body, M.; Legein, C.; Crosnier-Lopez, M.-P.; Galven, C.; Mauvy, F.; Durand, E.; Fourcade, S.; Sheptyakov, D.; Leblanc, M.; Maisonneuve, V.; Demourgues, A. Fluoride Solid Electrolytes: Investigation of the Tysonite-Type Solid Solutions La1−xBaxF3−x (x < 0.15). *Dalton Trans.* **2015**, *44* (45), 19625−19635.
(28) Rongeat, C.; Reddy, M. A.; Witter, R.; Fichtner, M. Solid Electrolytes for Fluoride Ion Batteries: Ionic Conductivity in Polycrystalline Tysonite-Type Fluorides. *ACS Appl. Mater. Interfaces* **2014**, *6* (3), 2103−2110.
(29) Dieudonné, B.; Chable, J.; Body, M.; Legein, C.; Durand, E.; Mauvy, F.; Fourcade, S.; Leblanc, M.; Maisonneuve, V.; Demourgues, A. The Key Role of the Composition and Structural Features in Fluoride Ion Conductivity in Tysonite Ce1−xSrxF3−x Solid Solutions. *Dalton Trans.* **2017**, *46* (11), 3761−3769.
(30) Chable, J.; Martin, A. G.; Bourdin, A.; Body, M.; Legein, C.; Jouanneaux, A.; Crosnier-Lopez, M.-P.; Galven, C.; Dieudonné, B.; Leblanc, M.; Demourgues, A.; Maisonneuve, V. Fluoride Solid Electrolytes: From Microcrystalline to Nanostructured Tysonite-Type La0.95Ba0.05F2.95. *J. Alloys Compd.* **2017**, *692*, 980−988.
(31) Mohammad, I.; Chable, J.; Witter, R.; Fichtner, M.; Reddy, M. A. Synthesis of Fast Fluoride-Ion-Conductive Fluorite-Type Ba1−XSbxF2+x ($0.1 \leq x \leq 0.4$): A Potential Solid Electrolyte for Fluoride-Ion Batteries. *ACS Appl. Mater. Interfaces* **2018**, *10* (20), 17249−17256.
(32) Grenier, A.; Porras-Gutierrez, A. G.; Body, M.; Legein, C.; Chrétien, F.; Raymundo-Piñero, E.; Dollé, M.; Groult, H.; Dambournet, D. Solid Fluoride Electrolytes and Their Composite with Carbon: Issues and Challenges for Rechargeable Solid State Fluoride-Ion Batteries. *J. Phys. Chem. C* **2017**, *121* (45), 24962−24970.
(33) Breuer, S.; Gombotz, M.; Pregartner, V.; Hanzu, I.; Wilkening, M. Heterogeneous F Anion Transport, Local Dynamics and Electrochemical Stability of Nanocrystalline La1−Ba F3−. *Energy Storage Mater.* **2019**, *16*, 481−490.
(34) Mohammad, I.; Witter, R.; Fichtner, M.; Anji Reddy, M. Room-Temperature, Rechargeable Solid-State Fluoride-Ion Batteries. *ACS Appl. Energy Mater.* **2018**, *1* (9), 4766−4775.
(35) Liu, L.; Yang, L.; Liu, M.; Li, X.; Shao, D.; Luo, K.; Wang, X.; Luo, Z. SnF2-Based Fluoride Ion Electrolytes MSnF4 (M = Ba, Pb) for the Application of Room-Temperature Solid-State Fluoride Ion Batteries. *J. Alloys Compd.* **2020**, *819*, No. 152983.
(36) Preishuber-Pflügl, F.; Epp, V.; Nakhal, S.; Lerch, M.; Wilkening, M. Defect-Enhanced F− Ion Conductivity in Layer-Structured Nanocrystalline BaSnF4 Prepared by High-Energy Ball Milling Combined with Soft Annealing. *Phys. Status Solidi C* **2015**, *12* (1−2), 10−14.
(37) Düvel, A.; Heitjans, P.; Fedorov, P.; Scholz, G.; Cibin, G.; Chadwick, A. V.; Pickup, D. M.; Ramos, S.; Sayle, L. W. L.; Sayle, E. K. L.; Sayle, T. X. T.; Sayle, D. C. Is Geometric Frustration-Induced Disorder a Recipe for High Ionic Conductivity? *J. Am. Chem. Soc.* **2017**, *139* (16), 5842−5848.
(38) Murakami, M.; Fujisaki, F.; Morita, Y. 19F/119Sn/207Pb NMR Studies on Phase Transition and Ion Dynamics in Cubic PbSnF4. *Solid State Ionics* **2020**, *355*, No. 115398.
(39) Wang, J.; Hao, J.; Duan, C.; Wang, X.; Wang, K.; Ma, C. A Fluoride-Ion-Conducting Solid Electrolyte with Both High Conductivity and Excellent Electrochemical Stability. *Small* **2022**, *18* (5), No. 2104508.
(40) Matsui, N.; Seki, T.; Suzuki, K.; Hirayama, M.; Kanno, R. Accelerated Exploration of Fast Fluoride-Ion Conductors Based on Compositional Descriptors. *ACS Appl. Energy Mater.* **2023**, *6* (22), 11663−11671.
(41) Davis, V. K.; Bates, C. M.; Omichi, K.; Savoie, B. M.; Momčilović, N.; Xu, Q.; Wolf, W. J.; Webb, M. A.; Billings, K. J.; Chou, N. H.; Alayoglu, S.; McKenney, R. K.; Darolles, I. M.; Nair, N. G.; Hightower, A.; Rosenberg, D.; Ahmed, M.; Brooks, C. J.; Miller, T. F.; Grubbs, R. H.; Jones, S. C. Room-Temperature Cycling of Metal Fluoride Electrodes: Liquid Electrolytes for High-Energy Fluoride Ion Cells. *Science* **2018**, *362* (6419), 1144−1148.
(42) Okazaki, K.-i.; Uchimoto, Y.; Abe, T.; Ogumi, Z. Charge−Discharge Behavior of Bismuth in a Liquid Electrolyte for Rechargeable Batteries Based on a Fluoride Shuttle. *ACS Energy Lett.* **2017**, *2* (6), 1460−1464.
(43) Preishuber-Pflügl, F.; Bottke, P.; Pregartner, V.; Bitschnau, B.; Wilkening, M. Correlated Fluorine Diffusion and Ionic Conduction in the Nanocrystalline F− Solid Electrolyte Ba0.6La0.4F2.4—19F T1(ρ) NMR Relaxation vs. Conductivity Measurements. *Phys. Chem. Chem. Phys.* **2014**, *16* (20), 9580−9590.
(44) Breuer, S.; Lunghammer, S.; Kiesl, A.; Wilkening, M. F Anion Dynamics in Cation-Mixed Nanocrystalline LaF3: SrF2. *J. Mater. Sci.* **2018**, *53* (19), 13669−13681.
(45) Dieudonné, B.; Chable, J.; Mauvy, F.; Fourcade, S.; Durand, E.; Lebraud, E.; Leblanc, M.; Legein, C.; Body, M.; Maisonneuve, V.; Demourgues, A. Exploring the Sm1−XCaxF3−x Tysonite Solid Solution as a Solid-State Electrolyte: Relationships between Structural Features and F− Ionic Conductivity. *J. Phys. Chem. C* **2015**, *119* (45), 25170−25179.
(46) Puin, W.; Rodewald, S.; Ramlau, R.; Heitjans, P.; Maier, J. Local and Overall Ionic Conductivity in Nanocrystalline CaF2. *Solid State Ionics* **2000**, *131* (1), 159−164.
(47) Mercadier, B.; Coles, S. W.; Duttine, M.; Legein, C.; Body, M.; Borkiewicz, O. J.; Lebedev, O.; Morgan, B. J.; Masquelier, C.; Dambournet, D. Dynamic Lone Pairs and Fluoride-Ion Disorder in Cubic-BaSnF4. *J. Am. Chem. Soc.* **2023**, *145* (43), 23739−23754.
(48) Fujisaki, F.; Mori, K.; Yonemura, M.; Ishikawa, Y.; Kamiyama, T.; Otomo, T.; Matsubara, E.; Fukunaga, T. Mechanical Synthesis and Structural Properties of the Fast Fluoride-Ion Conductor PbSnF4. *J. Solid State Chem.* **2017**, *253*, 287−293.
(49) Mori, K.; Mineshige, A.; Emoto, T.; Sugiura, M.; Saito, T.; Namba, K.; Otomo, T.; Abe, T.; Fukunaga, T. Electrochemical, Thermal, and Structural Features of BaF $_2$ − SnF $_2$ Fluoride-Ion

https://doi.org/10.1021/acs.chemmater.4c01644
Chem. Mater. 2024, 36, 8076−8087

Electrolytes. *J. Phys. Chem. C* **2021**, *125*, 12568−12577, DOI: 10.1021/acs.jpcc.1c03326.
(50) Dénès, G.; Birchall, T.; Sayer, M.; Bell, M. F. BaSnF4—A New Fluoride Ionic Conductor with the α-PbSnF4 Structure. *Solid State Ionics* **1984**, *13* (3), 213−219.
(51) Chen, H.; Aalto, T.; Vanita, V.; Clemens, O. Effect of Uniaxial Stack Pressure on the Performance of Nanocrystalline Electrolytes and Electrode Composites for All-Solid-State Fluoride-Ion Batteries. *Small Structures* **2024**, *5* (7), No. 2300570.
(52) Birchall, T.; Dénès, G.; Ruebenbauer, K.; Pannetier, J. A Neutron Diffraction And119Sn Mössbauer Study of PbSnF4 and BaSnF4. *Hyperfine Interact.* **1986**, *29* (1), 1331−1334.
(53) Chaudhuri, S.; Castiglione, M.; Wang, F.; Wilson, M.; Madden, P. A.; Grey, C. P. Study of Fluoride Ion Motions in PbSnF4 and BaSnF4 Compounds With Molecular Dynamics Simulation and Solid State NMR Techniques. *MRS Proc.* **2000**, *658* (1), No. 109.
(54) Chaudhuri, S.; Wang, F.; Grey, C. P. Resolving the Different Dynamics of the Fluorine Sublattices in the Anionic Conductor BaSnF4 by Using High-Resolution MAS NMR Techniques. *J. Am. Chem. Soc.* **2002**, *124* (39), 11746−11757.
(55) Patro, L. N.; Raju, N. R. C.; Meher, S. R.; Bharathi, K. K. Physical Properties of High Performance Fluoride Ion Conductor BaSnF4 Thin Films by Pulsed Laser Deposition. *Appl. Phys. A* **2013**, *112* (3), 727−732.
(56) Patro, L. N.; Hariharan, K. Influence of Synthesis Methodology on the Ionic Transport Properties of BaSnF4. *Mater. Res. Bull.* **2011**, *46* (5), 732−737.
(57) Zang, Z.; Liu, L.; Yang, L.; Luo, K.; Zou, C.; Chen, X.; Tao, X.; Luo, Z.; Chang, B.; Wang, X. Preparation and Performance of Eu $^{3+}$ -Doped BaSnF $_4$ -Based Solid-State Electrolytes for Room-Temperature Fluoride-Ion Batteries. *ACS Sustainable Chem. Eng.* **2021**, *9*, 12978−12989, DOI: 10.1021/acssuschemeng.1c04523.
(58) Ahmad, M. M.; Yamane, Y.; Yamada, K. Structure, Ionic Conduction, and Giant Dielectric Properties of Mechanochemically Synthesized BaSnF4. *J. Appl. Phys.* **2009**, *106* (7), No. 074106.
(59) Dénès, G.; Milova, G.; Madamba, M. C.; Perfiliev, M. Structure and Ionic Transport of PbSnF4 Superionic Conductor. *Solid State Ionics* **1996**, *86*−*88*, 77−82.
(60) Ito, Y.; Mukoyama, T.; Funatomi, H.; Yoshikado, S.; Tanaka, T. The Crystal Structure of Tetragonal Form PbSnF4. *Solid State Ionics* **1994**, *67* (3), 301−305.
(61) Aboulaich, A.; Bouchet, R.; Delaizir, G.; Seznec, V.; Tortet, L.; Morcrette, M.; Rozier, P.; Tarascon, J.-M.; Viallet, V.; Dollé, M. A New Approach to Develop Safe All-Inorganic Monolithic Li-Ion Batteries. *Adv. Energy Mater.* **2011**, *1* (2), 179−183.
(62) Chen, H.; Aalto, T.; Vanita, V.; Clemens, O. Effect of Uniaxial Stack Pressure on the Performance of Nanocrystalline Electrolytes and Electrode Composites for All-Solid-State Fluoride-Ion Batteries. *Small Struct.* **2024**, *5*, No. 2300570.
(63) Nadeina, A.; Rozier, P.; Seznec, V. Facile Synthesis of a Common Na-Ion Battery Cathode Material Na3V2(PO4)2F3 by Spark Plasma Sintering. *Energy Technol.* **2020**, *8* (5), No. 1901304.
(64) Lalère, F.; Leriche, J. B.; Courty, M.; Boulineau, S.; Viallet, V.; Masquelier, C.; Seznec, V. An All-Solid State NASICON Sodium Battery Operating at 200 °C. *J. Power Sources* **2014**, *247*, 975−980.
(65) Rodríguez-Carvajal, J. Recent Advances in Magnetic Structure Determination by Neutron Powder Diffraction. *Phys. B* **1993**, *192* (192), 55−69.
(66) Thompson, P.; Cox, D. E.; Hastings, J. B. Rietveld Refinement of Debye−Scherrer Synchrotron X-Ray Data from Al2O3. *J. Appl. Crystallogr.* **1987**, *20* (2), 79−83.
(67) Cussen, L. D.; Pappas, C.; Rhodes, N. J.; Schooneveld, E. M.; Sykora, G. J.; van Eijck, L.; van Well, A. A. Design and Performance of a Novel Neutron Powder Diffractometer: PEARL at TU Delft. *J. Appl. Crystallogr.* **2016**, *49* (5), 1398−1401.
(68) Massiot, D.; Fayon, F.; Capron, M.; King, I.; Le Calvé, S.; Alonso, B.; Durand, J.-O.; Bujoli, B.; Gan, Z.; Hoatson, G. Modelling One- and Two-Dimensional Solid-State NMR Spectra. *Magn. Reson. Chem.* **2002**, *40* (1), 70−76.
(69) Cavaliere, P.; Sadeghi, B.; Shabani, A. Spark Plasma Sintering: Process Fundamentals. In *Spark Plasma Sintering of Materials: Advances in Processing and Applications*; Cavaliere, P., Ed.; Springer International Publishing: Cham, 2019; pp 3−20.
(70) Motohashi, K.; Nakamura, T.; Kimura, Y.; Uchimoto, Y.; Amezawa, K. Influence of Microstructures on Conductivity in Tysonite-Type Fluoride Ion Conductors. *Solid State Ionics* **2019**, *338*, 113−120.
(71) Williamson, G. K.; Hall, W. H. X-Ray Line Broadening from Filed Aluminium and Wolfram. *Acta Metall.* **1953**, *1* (1), 22−31.
(72) Mikami, M.; Kinemuchi, Y.; Kubo, K.; Uchiyama, N.; Miyazaki, H.; Nishino, Y. Flash-Sintering of Antimony Telluride and Its Thermoelectric Properties. *J. Appl. Phys.* **2018**, *124* (10), No. 105104.
(73) Mikami, M.; Miyazaki, H.; Nishino, Y. Suppressed Atomic Diffusion in Flash Sintering of Bismuth Telluride. *J. Eur. Ceram. Soc.* **2022**, *42* (10), 4233−4238.
(74) Gao, N. F.; Li, J. T.; Zhang, D.; Miyamoto, Y. Rapid Synthesis of Dense Ti3SiC2 by Spark Plasma Sintering. *J. Eur. Ceram. Soc.* **2002**, *22* (13), 2365−2370.
(75) Jeong, K.; Lee, H.; Lee, C.; Wook, L. H.; Kim, H.; Lee, E.; Cho, M.-H. Ferroelectric Switching in GeTe through Rotation of Lone-Pair Electrons by Electric Field-Driven Phase Transition. *Appl. Mater. Today* **2021**, *24*, No. 101122.
(76) Matar, S. F.; Galy, J. Lone Electron Pair (E) Role on the Crystal Structures and the Mechanism of High Ionic Conductivity of PbSnF4E2. Stereochemical and Ab Initio Investigations. *Solid State Sci.* **2016**, *52*, 29−36.
(77) Biswal, M.; Body, M.; Legein, C.; Sadoc, A.; Boucher, F. NbF5 and TaF5: Assignment of 19F NMR Resonances and Chemical Bond Analysis from GIPAW Calculations. *J. Solid State Chem.* **2013**, *207*, 208−217.
(78) Banik, A.; Famprikis, T.; Ghidiu, M.; Ohno, S.; Kraft, M. A.; Zeier, W. G. On the Underestimated Influence of Synthetic Conditions in Solid Ionic Conductors. *Chem. Sci.* **2021**, *12* (18), 6238−6263.
(79) Schwietert, T. K.; Arszelewska, V. A.; Wang, C.; Yu, C.; Vasileiadis, A.; de Klerk, N. J. J.; Hageman, J.; Hupfer, T.; Kerkamm, I.; Xu, Y.; van der Maas, E.; Kelder, E. M.; Ganapathy, S.; Wagemaker, M. Clarifying the Relationship between Redox Activity and Electrochemical Stability in Solid Electrolytes. *Nat. Mater.* **2020**, *19* (4), 428−435.
(80) Zhu, Y.; He, X.; Mo, Y. Origin of Outstanding Stability in the Lithium Solid Electrolyte Materials: Insights from Thermodynamic Analyses Based on First-Principles Calculations. *ACS Appl. Mater. Interfaces* **2015**, *7* (42), 23685−23693.